

# Harnessing graph state resources for robust quantum magnetometry under noise

Phu Trong Nguyen,<sup>1</sup> Trung Kien Le,<sup>2,\*</sup> Hung Q. Nguyen,<sup>3</sup> and Le Bin Ho<sup>4,5,†</sup>

<sup>1</sup>*Department of Advanced Material Science and Nanotechnology,  
University of Science and Technology of Hanoi, Vietnam Academy of Science and Technology, Hanoi, Vietnam*

<sup>2</sup>*Department of Physics, University of California, Santa Barbara, Santa Barbara, USA*

<sup>3</sup>*Nano and Energy Center, University of Science,  
Vietnam National University, Hanoi, 120401, Vietnam*

<sup>4</sup>*Frontier Research Institute for Interdisciplinary Sciences, Tohoku University, Sendai 980-8578, Japan*

<sup>5</sup>*Department of Applied Physics, Graduate School of Engineering, Tohoku University, Sendai 980-8579, Japan*

(Dated: September 5, 2024)

Precise measurement of magnetic fields is essential for various applications, such as fundamental physics, space exploration, and biophysics. Although recent progress in quantum engineering has assisted in creating advanced quantum magnetometers, there are still ongoing challenges in improving their efficiency and noise resistance. This study focuses on using symmetric graph state resources for quantum magnetometry to enhance measurement precision by analyzing the estimation theory under time-homogeneous and time-inhomogeneous noise models. The results show a significant improvement in estimating both single and multiple Larmor frequencies. In single Larmor frequency estimation, the quantum Fisher information spans a spectrum from the standard quantum limit to the Heisenberg limit within a periodic range of the Larmor frequency, and in the case of multiple Larmor frequencies, it can exceed the standard quantum limit for both noisy cases. This study highlights the potential of graph state-based methods for improving magnetic field measurements under noisy environments.

## I. INTRODUCTION

Quantum sensing utilizes quantum resources like non-classical states, entanglement, and squeezing to improve sensor capabilities beyond classical approaches [1]. Recent advances in quantum resource theory have been made in quantum-enhanced sensing using non-classical states [2–4], entangled cluster and graph states [5–8], many-body nonlocality and multiqubit systems [9–11], and squeezed resources [12–15]. Furthermore, various techniques like machine learning algorithms [16–20], quantum error correction methods [21–24], network sensing [25, 26], and hybrid algorithms [8, 27–32], are being explored for enhancing noise resilience and extracting insights from quantum sensing.

In quantum magnetometry, the precise measurement of magnetic fields is crucial in various subjects like fundamental physics research, space exploration, material science, geophysics, and medical biophysics. Recent advances in quantum engineering have led to the development of various quantum magnetometers, such as superconducting quantum interference device (SQUID) [33], diamond-based magnetometer [34, 35], single-spin quantum magnetometer [36], submicron-scale NMR spectroscopy [37], cold atom magnetometer [38], and 2D hexagonal boron nitride magnetic sensor [39]. These innovations find applications in highly sensitive and broadband magnetic field measurements [34, 35], scanning gradiometry [36], low magnetic fields [37], navigation [38],

and magnetic field imaging [39].

Improving the sensitivity of magnetometers is essential for different applications. However, the present methods are insufficient due to high quantum resource efficiency and noise resilience demands. Therefore, there is an urgent requirement for a novel resource that can enable the full potential of quantum magnetometry while being practical for experimental implementation.

Among various candidates, graph states have emerged as a promising avenue in the quest for quantum-enhanced magnetometry. Graph states are particular types of entangled states that can be represented by a graph, where the vertices represent qubits, and the edges represent entangling gates between the qubits [40, 41]. Due to their multipartite entanglement, they have demonstrated great potential in quantum computation [42, 43], communication [42, 44], and metrology [6–8]. Within the context of quantum magnetometry, harnessing the capabilities of graph states introduces a novel dimension to the quest for precision and robustness in the presence of noise.

This work explores symmetric graph state resources for robust quantum magnetometry under time-homogeneous and time-inhomogeneous noises [45]. Our approach begins by modeling an ensemble of  $N$  spin-1/2 particles as a sensor probe for measuring Larmor frequencies of an external magnetic field. Initially, the probe state is set up in a star-graph configuration, where one vertex (spin particle) is connected to the remaining  $N - 1$  vertices through CZ gates. We study the influence of noise in the model by analyzing the measurement precision from the perspective of estimation theory and quantum Fisher information.

For uncorrelated probes, the variance of estimating a single phase  $\phi$  follows  $\Delta^2\phi = \mathcal{O}(N^{-1})$ , commonly re-

\* Current address: Department of Applied Physics, Stanford University, Stanford, USA

† Electronic address: binho@fris.tohoku.ac.jp

ferred to as the standard quantum limit (SQL), whereas for entangled probes, it is possible to reach the Heisenberg limit (HL), where  $\Delta^2\phi = \mathcal{O}(N^{-2})$  [46–48]. However, under time-homogeneous noise, entangled sensors cannot surpass the SQL [49, 50]. In the presence of time-inhomogeneous noise, the variance can reach  $\Delta^2\phi = \mathcal{O}(N^{-1.5})$  [51–53], and similar results have been observed in the context of multiphase sensing [8, 45].

In our investigation for single Larmor frequency estimation, we observe a transition from SQL to HL behavior for a periodic range of the Larmor frequency. For multiple Larmor frequencies, we find that the variance  $\Delta^2\phi$  can beat the SQL for both time-homogeneous and time-inhomogeneous noise sources. This marks the initial instance where we observe surpassing the SQL under time-homogeneous noise. Our analysis of quantum magnetometry in these noise factors sheds light on the resilience and potential of graph state-based approaches for conducting highly precise magnetic field measurements in challenging and real-world conditions.

## II. RESULTS

### A. Measurement model and its initialization

Let us consider the measurement of an external magnetic field by employing a spin-1/2 system comprising  $N$  particles as the probing mechanism. Each particle interacts with the field and provide information about the field strengths. The coupling Hamiltonian is given by [54]

$$\mathcal{H} = - \sum_{k=1}^N \left( \boldsymbol{\mu}^{(k)} \cdot \mathbf{B} \right), \quad (1)$$

where  $\boldsymbol{\mu}^{(k)} = \frac{1}{2}\gamma_e\boldsymbol{\sigma}^{(k)}$  represents the magnetic moment of the  $k^{\text{th}}$  spin.  $\gamma_e$  denotes the gyromagnetic ratio, and  $\boldsymbol{\sigma}^{(k)} = (\sigma_x^{(k)}, \sigma_y^{(k)}, \sigma_z^{(k)})$  refers to the Pauli matrices. Here,  $\mathbf{B} = (B_x, B_y, B_z)$  signifies the external magnetic field. We define  $\phi_j = |\gamma_e|B_j$  for all  $j \in x, y, z$  as the Larmor frequency [54], and  $J_j = \frac{1}{2}\sum_k \sigma_j^{(k)}$  as the angular momentum. With this, the Hamiltonian recasts as

$$\mathcal{H} = \boldsymbol{\phi} \cdot \mathbf{J}, \quad (2)$$

where  $\boldsymbol{\phi} = (\phi_x, \phi_y, \phi_z)$  represents the set of Larmor frequencies requiring estimation, and  $\mathbf{J} = (J_x, J_y, J_z)$  are three components of the collective angular momentum. Refer to the Methods section for a detailed model and its quantum circuit.

The probe is initialized as a graph state, which typically consists of a collection of vertices denoted by  $V$  and edges represented by  $E$  as

$$G(V, E) = \prod_{i,j \in E} \text{CZ}_{ij} |+\rangle^{\otimes V}, \quad (3)$$

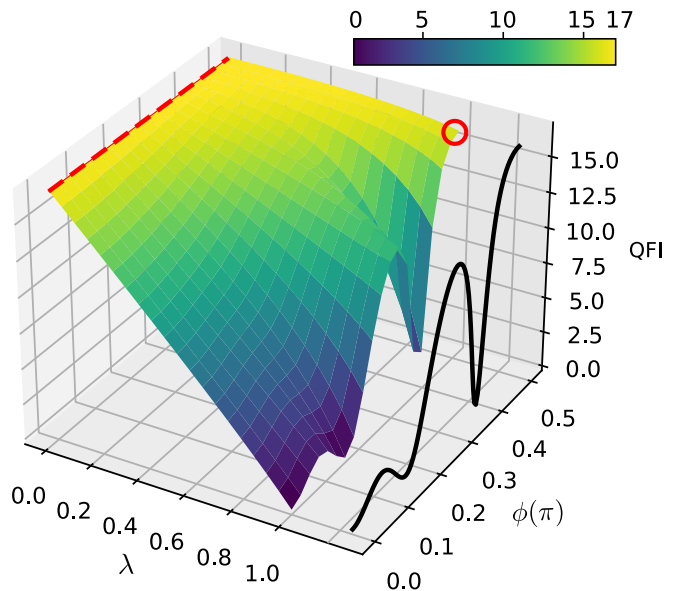


FIG. 1. **Quantum Fisher information in a single phase estimation.** Plot of QFI vs the noise probability  $\lambda$  and Larmor frequency  $\phi$  for  $N = 5$  and  $t = 1$ . For  $\lambda = 0$ , the QFI reaches  $Q = (N - 1)^2 + 1 \forall \phi$  (dashed red line). Increasing  $\lambda$ , the QFI gradually reduces and reaches the minimum at  $\lambda = 1$ . Remarkably, this minimum is non-zero for a non-zero  $\phi$  as illustrated by the soiled black curve. For  $\phi = \pi/2$ , it is given by  $(N - 1)^2$  (red circle).

where  $\text{CZ}_{ij}$  represents the controlled-Z gate connecting the  $i^{\text{th}}$  and  $j^{\text{th}}$  spins, and  $|+\rangle$  is an element in the basis of Pauli  $\sigma_x$ . Graph states serve as valuable assets in quantum metrology [6, 8], as demonstrated by their application in achieving Heisenberg scaling, as observed with star configurations where the quantum Fisher information (QFI) gives  $(N - 1)^2 + 1$ , and with local Clifford (LC) operations where the QFI gives  $N^2$  [6]. Hereafter, we examine the impact of graph-state resources on quantum-enhanced magnetometry within a noisy environment.

### B. Single phase estimation

We examine the estimation of a single Larmor frequency denoted as  $\boldsymbol{\phi} = (\phi, 0, 0)$ . The coupling Hamiltonian is  $\mathcal{H} = \phi J_x$ , and the corresponding unitary operator is expressed as

$$\mathcal{U}(\phi) = \exp(-it\phi J_x). \quad (4)$$

The initial probe state is prepared in a graph configuration  $\rho_0 = |G\rangle\langle G|$ . After the interaction, it evolves to  $\rho(\phi) = \mathcal{U}(\phi)\rho_0\mathcal{U}^\dagger(\phi)$ . During the magnetic field coupling, the probe interacts with its surroundings and decoheres. Our analysis focuses on dephasing noise as a type of phase

decoherence that leads to the evolution of the state

$$\rho(\phi, \gamma) = \left[ \prod_{k=1}^N e^{\gamma t \mathcal{L}^{(k)}} \right] \rho(\phi), \quad (5)$$

where  $\gamma$  is the dephasing rate. Dephasing is often referred to as the spin-spin relaxation process [55], which affects the relative phase in the probe's basis and can be represented by the Pauli operator  $\sigma_z$ . By employing the Kraus operators to account for dephasing noise as  $\mathcal{K}_0 = \text{diag}(1, \sqrt{1-\lambda})$ ,  $\mathcal{K}_1 = \text{diag}(0, \sqrt{\lambda})$ , we obtain

$$e^{\gamma t \mathcal{L}^{(k)}} \rho(\phi) = \mathcal{K}_0^{(k)} \rho(\phi) [\mathcal{K}_0^{(k)}]^\dagger + \mathcal{K}_1^{(k)} \rho(\phi) [\mathcal{K}_1^{(k)}]^\dagger, \quad (6)$$

where  $\lambda = 1 - e^{-\gamma t} \in [0, 1]$  is the dephasing probability. For other noisy scenarios, please see the Methods section.

The final state  $\rho(\phi, \gamma)$  contains detailed information about the unknown Larmor frequency  $\phi$ . To evaluate the precision of the estimation, we examine the QFI  $Q$ . By decomposing  $\rho(\phi, \gamma) = \sum_k \ell_k |\ell_k\rangle\langle\ell_k|$ , the QFI yields [56]

$$Q = 2 \sum_{i,j,\ell_i+\ell_j \neq 0} \frac{|\langle \ell_i | \partial_\phi \rho(\phi, \gamma) | \ell_j \rangle|^2}{\ell_i + \ell_j}. \quad (7)$$

For numerical calculation, let us fix the sensing time  $t = 1$  in an arbitrary unit. The results are presented in Fig. 1, focusing on the star-graph configuration and using  $N = 5$  as an illustrative example. In the absence of noise, i.e.,  $\lambda = 0$ , the QFI yields [6]

$$Q = 4 \left[ \langle G | J_x^2 | G \rangle - (\langle G | J_x | G \rangle)^2 \right] = (N-1)^2 + 1, \quad (8)$$

which does not depend on  $\phi$  as shown in the dashed red line. See the Methods section for detailed calculation.

In the presence of noise, the QFI depends on both  $\lambda$  and  $\phi$ . As  $\lambda$  increases, the QFI gradually decreases, reaching its minimum value at  $\lambda = 1$ . Interestingly, this minimum value remains nonzero for  $\phi \neq 0$ , which is demonstrated by the solid black curve. Specifically, for  $\phi = \pi/2$ , the QFI is even by  $(N-1)^2$  (red circle). See the Methods section for detailed calculation.

A specific case of star graph is a GHZ state up to a local unitary (LU) transformation [41, 57]. Let us consider the initial probe state to be a GHZ state

$$|\psi\rangle_{\text{GHZ}} = \frac{1}{\sqrt{2}} (|\nu_{\text{max}}\rangle + |\nu_{\text{min}}\rangle), \quad (9)$$

where  $|\nu_{\text{max}}\rangle$  and  $|\nu_{\text{min}}\rangle$  are eigenstates of  $J_x$  corresponding to the maximum and minimum eigenvalues  $\nu_{\text{max}}$  and  $\nu_{\text{min}}$ , respectively. Particularly, this state can be prepared by applying a Hadamard gate to the first spin particle of the star graph state in Eq. (25). The QFI gives (see the Methods section)

$$Q_{\text{GHZ}} = 4 \left[ \langle \psi_{\text{GHZ}} | J_x^2 | \psi_{\text{GHZ}} \rangle - (\langle \psi_{\text{GHZ}} | J_x | \psi_{\text{GHZ}} \rangle)^2 \right] = N^2. \quad (10)$$

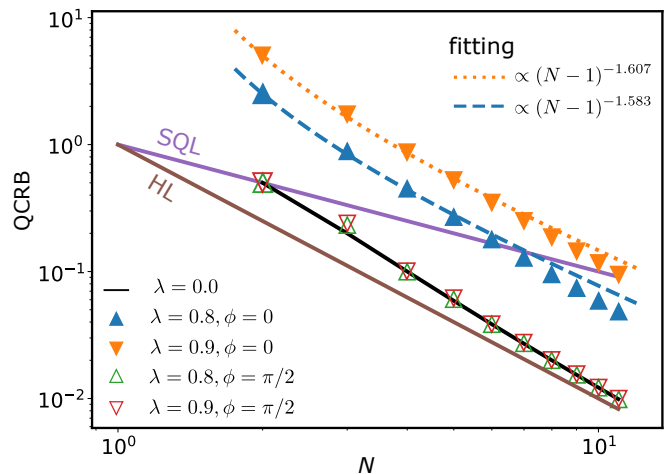


FIG. 2. **Quantum Cramér-Rao bound in a single phase estimation.** The plot of QCRB as a function of the number of spins  $N$  for various  $\lambda$  and  $\phi$ . Additionally, SQL and HL are displayed for comparative purposes. The plot is presented with the star-graph configuration.

Here, the QFI remains independent of  $\phi$ . Upon closer examination, it becomes evident that the QFI attains the Heisenberg limit of  $N^2$  in the absence of noise. In the presence of dephasing noise, the QFI is invariant, preserving its  $N^2$  as detailed in the Methods section. This result is trivial as noise primarily affects the phase or coherence of quantum states along the  $z$ -axis, while GHZ here points toward the  $x$ -axis.

Next, we examine the quantum Cramér-Rao bound (QCRB) for various values of  $N$ . It is the ultimate bound that imposes the precision achievable in the estimation process, i.e.,  $M \cdot \Delta^2 \phi \geq C_F \geq C_Q$ , where  $\Delta^2 \phi = \langle (\phi - \hat{\phi})^2 \rangle - \langle \phi - \hat{\phi} \rangle^2$  is the variance of  $\phi$ , which indicates the difference between the true value  $\phi$  and its estimated counterpart  $\hat{\phi}$ ,  $M$  is the repeated experiments. Here,  $C_F$  and  $C_Q$  are classical and quantum Cramér-Rao bound, respectively. The QCRB is determined through the inversion of the QFI as

$$C_Q = Q^{-1}, \quad (11)$$

which can be achieved in the single-phase estimation, such as using a Bayesian estimator or neural network technique (see [20] and Refs therein).

The numerical results are showcased in Fig. 2. For  $\phi = 0$ , the QCRB can beat the SQL event for large noise. Here we illustrate for  $\lambda = 0.8$  ( $\blacktriangle$ ) and  $0.9$  ( $\blacktriangledown$ ), and the fitting curves are proportional to  $(N-1)^{-1.583}$  (blue dashed line) and  $(N-1)^{-1.607}$  (orange dotted line), respectively. Throughout the paper, we use the fitting function as  $f(N) = a(N-1)^b \forall a, b \in \mathcal{R}$ , which is inspired by the exact result when  $\lambda = 0$ . For  $\phi = \pi/2$ , the analytical findings in Fig. 1 suggest that the QCRB fluctuates between  $\frac{1}{(N-1)^2+1}$  and  $\frac{1}{(N-1)^2}$  for  $\lambda \in [0, 1]$ . Comparatively, the cases of  $\lambda = 0.8$  ( $\triangle$ ) and  $0.9$  ( $\nabla$ ) align closely with the  $\lambda = 0$  scenario (the black line), exhibiting

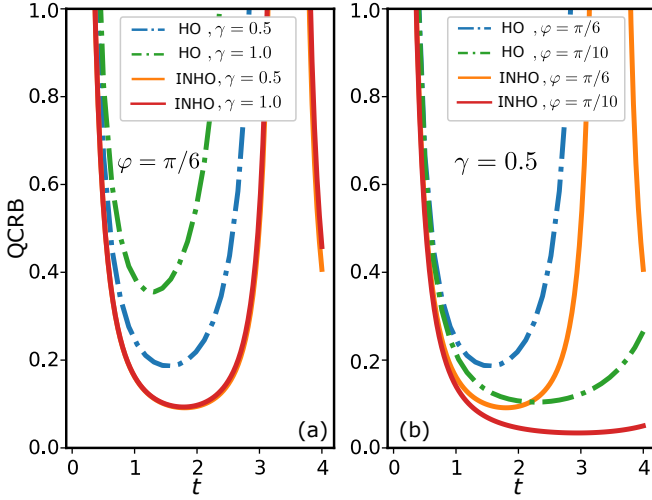


FIG. 3. **Quantum Cramér-Rao bound in a multiphase estimation.** The plot of QCRB as a function of sensing time for time-homogeneous (HO) and time-inhomogeneous (INHO) noises. Here we fixed the Larmor frequencies  $\phi_x = \phi_y = \phi_z \equiv \varphi = \pi/6$  in (a) and fixed  $\gamma = 0.5$  in (b). The QCRB initially decreases, reaches a minimum, and then increases with increasing sensing time.

a remarkable match. Notably, they attain the Heisenberg scaling. For comparison, we show the standard quantum limit  $\text{SQL} = N^{-1}$  and the Heisenberg limit  $\text{HL} = N^{-2}$ . This result represents an advanced approach in leveraging graph states for robust sensing in noisy environments, indicating a transition from the SQL to the HL within a periodic range of the Larmor frequency.

### C. Multiple phases estimation

We consider the estimation of Larmor frequencies as  $\phi = (\phi_x, \phi_y, \phi_z)$  with the coupling Hamiltonian being given in Eq. (2). The unitary evolution yields

$$\mathcal{U}(\phi) = \exp(-it\phi \cdot \mathbf{J}). \quad (12)$$

We consider the Ornstein-Uhlenbeck noise model, originating from the stochastic fluctuations of the external magnetic field [58]. The noise is characterized by Kraus operators [59]

$$\mathcal{K}_0(t) = \text{diag}(1, \sqrt{1-q(t)}), \mathcal{K}_1(t) = \text{diag}(0, \sqrt{q(t)}), \quad (13)$$

where  $q(t) = 1 - e^{-f(t)}$  and  $f(t) = \gamma[t + \tau_c(e^{-t/\tau_c} - 1)]$ . Here,  $\tau_c$  is the memory time of the environment. In the limit of time-homogeneous behavior or white noise limit ( $\tau_c \rightarrow 0$ ), we have  $f(t) = \gamma t$ , which corresponds to the previous dephasing case. In the time-inhomogeneous case, the time  $\tau_c$  is large, and thus  $t/\tau_c \ll 1$  (short-time limit). In this case, the expression becomes  $f(t) = \frac{\gamma t^2}{2\tau_c}$ .

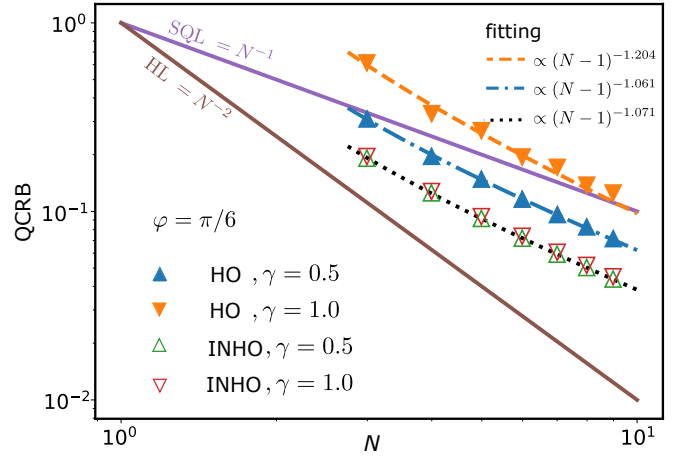


FIG. 4. **Quantum Cramér-Rao bound in a multiphase estimation.** The plot of QCRB vs  $N$  at fixed Larmor frequencies  $\phi_x = \phi_y = \phi_z \equiv \varphi = \pi/6$  for two cases of time-homogeneous and time-inhomogeneous noises.

The function  $q(t)$  is defined as

$$q(t) = \begin{cases} 1 - \exp(-\gamma t) & \text{time-homogeneous,} \\ 1 - \exp(-\frac{\gamma t^2}{2\tau_c}) & \text{time-inhomogeneous.} \end{cases} \quad (14)$$

In the numerical simulation,  $\tau_c$  is fixed at  $\tau_c = 20$  for the time-inhomogeneous case.

Similar as the single phase case, we first calculate  $\rho(\phi) = \mathcal{U}(\phi)|G\rangle\langle G|\mathcal{U}^\dagger(\phi)$ , and then derive  $\rho(\phi, \gamma)$  by applying the Kraus operators in Eq. (13) for all qubits. Next, given the decomposed form as  $\rho(\phi, \gamma) = \sum_k \ell_k |\ell_k\rangle\langle \ell_k|$ , the quantum Fisher information matrix (QFIM) gives

$$Q_{\alpha\beta} = 2 \sum_{i,j, \ell_i + \ell_j \neq 0} \frac{\langle \ell_i | \partial_{\phi_\alpha} \rho(\phi, \gamma) | \ell_j \rangle \langle \ell_j | \partial_{\phi_\beta} \rho(\phi, \gamma) | \ell_i \rangle}{\ell_i + \ell_j}, \quad (15)$$

and the QCRB in the multiphase case is given by  $\text{C}_Q = \text{Tr}[Q^{-1}]$ . See detailed calculations in the Methods section.

Figure 3 illustrates the QCRB concerning time-homogeneous and time-inhomogeneous noises as a function of time  $t$ . Consistent with findings reported in [8, 45], a pivotal insight surfaces: an optimal sensing time emerges leads to minimized CRBs across the examined scenarios. For time-homogeneous (HO) noise, the optimal sensing time tends to be shorter, whereas for time-inhomogeneous (INHO) noise, an extended sensing time is favored. Remarkably, the presence of time-inhomogeneous dephasing yields lower metrological bounds compared to the time-homogeneous counterpart.

In Figure 4, we can observe the minimum QCRB for various values of  $N$ . The results demonstrate that as  $N$  increases, time-inhomogeneous noise consistently outperforms the SQL across all levels of noise (represented by

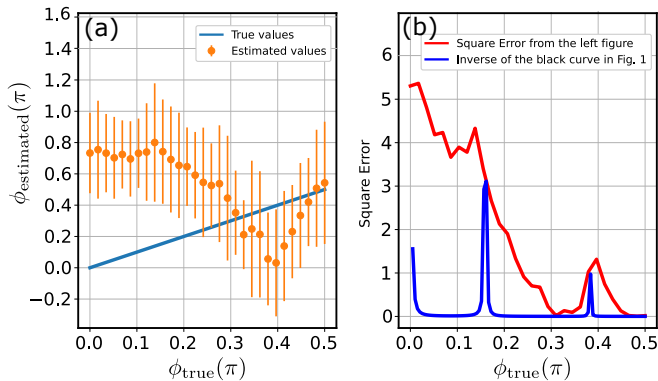


FIG. 5. **Bayesian inference.** (a) A comparison between true and estimated values. The true values are represented by the blue line where  $\phi_{\text{true}} = \phi_{\text{estimated}}$ . The estimated values are indicated by orange dots along with error bars, derived from 100 repeated experiments using Bayesian inference. (b) Plot of squared errors as a function of  $\phi$  and their comparison with the inverse QFI extracted from the black curve in Fig. 1. These results are presented for  $\lambda = 1$ .

open triangles). The relationship follows a fitted function that scales as  $\propto (N-1)^{-1.071}$ . Similarly, in the case of time-homogeneous noise, the bounds tend to surpass the SQL as  $N$  grows larger. This is the first instance we observe exceeding the SQL under time-homogeneous noise.

### III. DISCUSSION

We discuss the Bayesian inference in estimating the single Larmor frequency. In this approach, the process

begins with defining a likelihood function that expresses the probability of the observed data set  $\{D\}$  concerning the parameter of interest  $\phi$ . In our scenario, the likelihood function is calculated as the product of probabilities while measuring the final state  $\rho(\phi, \gamma)$  in Eq. (5) with the computational bases  $\{|k\rangle\}$  as

$$P(D|\phi) = \prod_{k=1}^{2^N} \text{Tr}[\rho(\phi, \gamma)|k\rangle\langle k|]. \quad (16)$$

The Bayesian theorem is then applied to compute the posterior distribution, which describes the uncertainty associated with the parameter as

$$P(\phi|D) = \frac{P(D|\phi)}{\int P(D|\phi)d\phi}. \quad (17)$$

Finally, the estimated phase is given by

$$\phi_{\text{estimated}} = \int \phi P(\phi|D)d\phi. \quad (18)$$

Practically, sampling techniques such as Markov Chain Monte Carlo (MCMC) or Nested Sampling (NS) are used to generate samples from the posterior distribution [20]. These samples are then used for estimates, typically as the posterior mean or credible intervals. These estimates convey not only the point estimate but also the related uncertainty.

To illustrate, we focus on the case where  $\lambda = 1$  and proceed to theoretically derive the likelihood function (16) using  $\rho_N(\phi)$  from Eq.(35). It gives

$$\begin{aligned} P(D|\phi) &= \prod_{k=1}^{2^N} \text{Tr}[\rho_N(\phi)|k\rangle\langle k|] \\ &= \frac{1}{2^{N \cdot (2^N)}} \sum_{k=0}^{2^N-1} \binom{2^N-1}{k} (-1)^k \sin^{2k}(\phi) \sin^{2k}[(N-1)\phi], \end{aligned} \quad (19)$$

Then  $P(\phi|D)$  yields

$$P(\phi|D) = \frac{1}{2^{N \cdot (2^N)}} \sum_{k=0}^{2^N-1} \binom{2^N-1}{k} (-1)^k \int \sin^{2k}(\phi) \sin^{2k}[(N-1)\phi]d\phi. \quad (20)$$

Finally, we obtain

$$\phi_{\text{estimated}} = \int \phi P(\phi|D)d\phi. \quad (21)$$

The detailed calculation for obtaining the estimated  $\phi_{\text{estimated}}$  is provided in the Methods section. We present

our findings in Fig. 5. In (a), a comparison is made between the true values and the estimated values. The true values are represented by the blue line when  $\phi_{\text{true}} = \phi_{\text{estimated}}$ . The average estimated values are indicated by orange dots with error bars, obtained through the Bayesian inference method from  $M = 100$  repeated ex-



periments in a quantum circuit. In (b), we plot the squared error  $\Delta^2\phi$  as a function of  $\phi$  and compare it with the inverse QFI extracted from the black curve in Fig. 1 after re-scaling, i.e.,  $2.5 \times \frac{1}{MQ}$ . It indicates the QCRB relation as  $\Delta^2\phi \geq \frac{1}{MQ}$ .

## IV. METHODS

### A. Qubits model

We introduce a measurement model using qubits system as shown in Fig. (6). In metrology schemes, we measure a system by using a probe that couples to it. After the interaction, we measure the probe to estimate the system's information. In our model, the system is the magnetic field, and the probe is an ensemble of spins. When considering noise, it couples to the probe, and this coupling is different from the system-probe interaction. In our case, we consider dephasing and Ornstein-Uhlenbeck noise models. Dephasing is often referred to as the spin-spin relaxation process. It affects the relative phase in the probe's basis, which can be represented by the Pauli operator  $\sigma_z$ . The noise occurs during the interaction process between the system and the probe. Initially, at  $t = 0$ , we turn on the coupling between the probe and the system. At time  $t = t_f$ , we turn off the interaction and measure the probe. Assuming the preparation and measurement times are very short, the probe does not evolve before time  $t = 0$  and after  $t = t_f$ . Thus, noise only affects the probe during the interaction time. The measurement scheme is given in Fig. (6)a.

For the interaction, we first rewrite Eq. (12) as

$$\begin{aligned} \mathcal{U}(\phi) &= \exp \left[ -it(\phi_x J_x + \phi_y J_y + \phi_z J_z) \right] \\ &= \exp \left[ -it \sum_{k=1}^N \left( \frac{\phi_x}{2} \sigma_x^{(k)} + \frac{\phi_y}{2} \sigma_y^{(k)} + \frac{\phi_z}{2} \sigma_z^{(k)} \right) \right] \\ &= \prod_{k=1}^N \exp \left[ -it \left( \frac{\phi_x}{2} \sigma_x^{(k)} + \frac{\phi_y}{2} \sigma_y^{(k)} + \frac{\phi_z}{2} \sigma_z^{(k)} \right) \right]. \end{aligned} \quad (22)$$

We set a single-qubit unitary as

$$\mathcal{U}_1(\phi) = \exp \left[ -it \left( \frac{\phi_x}{2} \sigma_x + \frac{\phi_y}{2} \sigma_y + \frac{\phi_z}{2} \sigma_z \right) \right], \quad (23)$$

and apply it to all qubits in a quantum circuit. For a single-phase estimation, it becomes a rotation gate, i.e.  $\mathcal{U}_1(\phi) = \exp \left[ -it \frac{\phi_x}{2} \sigma_x \right]$ .

The quantum circuit is given in Fig. 6b. The first block is the graph state generation with star configuration, wherein a Hadamard gate is applied to each qubit initially set in the state  $|0\rangle$ , transforming them into  $|+\rangle$  states. These qubits are connected as a star, with the

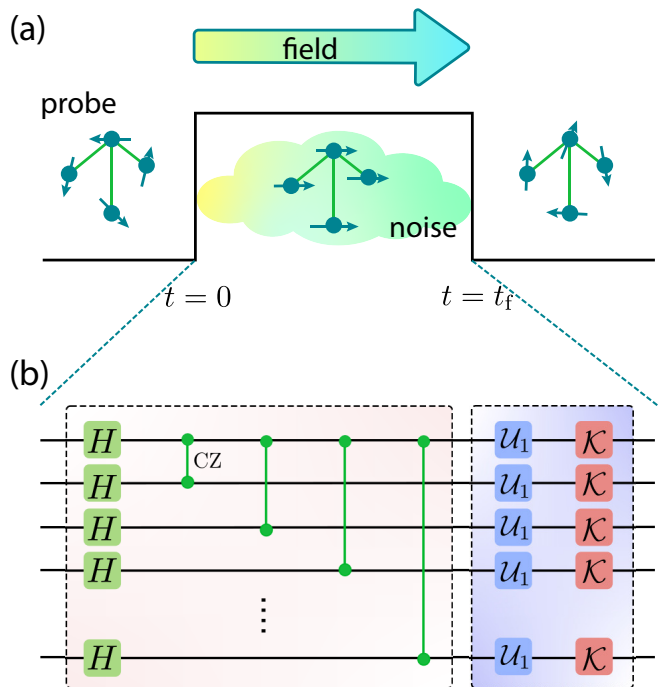


FIG. 6. (a): Quantum magnetometry scheme with noise model. The probe is an ensemble of spins prepared in a graph state. The probe interacts with an external field during the time  $t = 0$  to  $t = t_f$ . The noise also appears during the interaction time. (b) The quantum circuit designed for quantum magnetometry. The first block is a star configuration, applying Hadamard gates to  $|0\rangle$  qubits to transform them into  $|+\rangle$  states and connecting them as a star, with the first qubit at the center linked to the surrounding qubits via CZ gates. The second block involves phase and noise encoding using  $\mathcal{U}_1(\phi)$ , followed by Kraus operators  $\mathcal{K} = (\mathcal{K}_0, \mathcal{K}_1)$  apply to all qubits.

first qubit at the center and connects to the surrounding qubits through CZ gates. The second block is phase and noise encoding, given by applying  $\mathcal{U}_1(\phi)$  and followed by the Kraus operators  $\mathcal{K} = (\mathcal{K}_0, \mathcal{K}_1)$  apply to all qubits. The final state is used to calculate quantum Fisher information (QFI) for single phase estimation and quantum Fisher information matrix (QFIM) for multiphase estimation. From these, we derive the corresponding QCRB [60].

### B. Deriving QFI for single parameter estimation

#### 1. For star graph state

We first calculate the QFI with the initial star graph state in the case of without noise. We express the QFI in terms of its generator as

$$Q = 4\langle \Delta \mathcal{H}_\phi^2 \rangle = 4 \left[ \langle G | \mathcal{H}_\phi^2 | G \rangle - (\langle G | \mathcal{H}_\phi | G \rangle)^2 \right], \quad (24)$$

where  $\mathcal{H}_\phi = i\mathcal{U}^\dagger(\phi)\partial_\phi\mathcal{U}(\phi)$ . For single-phase estimation, it gives  $\mathcal{H}_\phi = J_x = \frac{1}{2} \sum_{k=1}^N \sigma_x^{(k)}$ .

To calculate Eq. (24), we first expand the graph state to a star configuration, with one central qubit (qubit 1) connects to the remaining surrounding  $N - 1$  qubits:

$$\begin{aligned} |G\rangle &= \prod_{k=2}^N \text{CZ}_{1,k} |+\rangle^{\otimes N} \\ &= \left( \text{CZ}_{1,N} \text{CZ}_{1,N-1} \cdots \text{CZ}_{1,2} \right) |+\rangle^{\otimes N} \\ &= \frac{1}{\sqrt{2}} \left( |0\rangle|+\rangle^{\otimes(N-1)} + |1\rangle|-\rangle^{\otimes(N-1)} \right). \end{aligned} \quad (25)$$

Next, we compute  $\mathcal{H}_\phi |G\rangle$ :

$$\begin{aligned} \mathcal{H}_\phi |G\rangle &= \left[ \frac{1}{2} \sum_{k=1}^N \sigma_x^{(k)} \right] |G\rangle \\ &= \frac{1}{2\sqrt{2}} \left[ \left( |1\rangle|+\rangle^{\otimes(N-1)} + |0\rangle|-\rangle^{\otimes(N-1)} \right) + \right. \\ &\quad \left. (N-1) \left( |0\rangle|+\rangle^{\otimes(N-1)} - |1\rangle|-\rangle^{\otimes(N-1)} \right) \right]. \end{aligned} \quad (26)$$

Using Eq. (26), the first term in Eq. (24) gives:

$$\langle G | \mathcal{H}_\phi^2 | G \rangle = \langle G | \mathcal{H}_\phi \mathcal{H}_\phi | G \rangle = \frac{1}{4} \left( 1 + (N-1)^2 \right). \quad (27)$$

Using Eqs. (25,26), the second term in Eq. (24) yields

$$\langle G | \mathcal{H}_\phi | G \rangle^2 = 0. \quad (28)$$

As a result, the QFI in (24) gives

$$Q = 1 + (N-1)^2, \quad (29)$$

and the corresponding QCRB is  $C_Q = \frac{1}{Q} = \frac{1}{1+(N-1)^2}$ .

Now, we calculate the QFI under dephasing noise. We first recast the unitary Eq. (4) as

$$\begin{aligned} \mathcal{U}(\phi) &= \left[ \exp \left( -i \frac{\phi}{2} \sigma_x \right) \right]^{\otimes N} \\ &= \left[ \cos(\phi') I - i \sin(\phi') \sigma_x \right]^{\otimes N}, \end{aligned} \quad (30)$$

where we fixed  $t = 1$  and set  $\phi' = \phi/2$ . The initial graph state  $|G\rangle$  evolves to

$$\begin{aligned} |G(\phi)\rangle &= \left[ \cos(\phi') I - i \sin(\phi') \sigma_x \right]^{\otimes N} \cdot \frac{1}{\sqrt{2}} \left( |0\rangle|+\rangle^{\otimes(N-1)} + |1\rangle|-\rangle^{\otimes(N-1)} \right) \\ &= \frac{1}{\sqrt{2}} \left\{ \left( \cos(\phi') |0\rangle - i \sin(\phi') |1\rangle \right) \otimes e^{-i\phi'(N-1)} |+\rangle^{\otimes(N-1)} + \right. \\ &\quad \left. \left( \cos(\phi') |1\rangle - i \sin(\phi') |0\rangle \right) \otimes e^{i\phi'(N-1)} |-\rangle^{\otimes(N-1)} \right\} \\ &= \frac{1}{\sqrt{2}} \left\{ e^{-i\phi'(N-1)} \begin{pmatrix} \cos \phi' \\ -i \sin \phi' \end{pmatrix} \otimes |+\rangle^{\otimes(N-1)} + e^{i\phi'(N-1)} \begin{pmatrix} -i \sin \phi' \\ \cos \phi' \end{pmatrix} \otimes |-\rangle^{\otimes(N-1)} \right\}. \end{aligned} \quad (31)$$

The single-qubit dephasing is represented by Kraus operators  $\mathcal{K}_0 = \text{diag}(1, \sqrt{1-\lambda})$ ,  $\mathcal{K}_1 = \text{diag}(0, \sqrt{\lambda})$ . They act on a qubit  $i$  as  $\mathcal{K}_0^{(i)} = I \otimes \cdots \mathcal{K}_0 \cdots \otimes I$  and  $\mathcal{K}_1^{(i)} = I \otimes \cdots \mathcal{K}_1 \cdots \otimes I$ . Under dephasing, the quantum state (6) explicitly gives

$$\rho_k(\phi) = \mathcal{K}_0^{(k)} \rho_{(k-1)}(\phi) [\mathcal{K}_0^{(k)}]^\dagger + \mathcal{K}_1^{(k)} \rho_{(k-1)}(\phi) [\mathcal{K}_1^{(k)}]^\dagger, \quad (32)$$

for  $k = 1, \dots, N$  with  $\rho_0(\phi) = |G(\phi)\rangle\langle G(\phi)|$ .

To simplify the calculation, we focus on the maximum

noise probability,  $\lambda = 1$ . We first calculate

$$\begin{aligned} \rho_1(\phi) &= \mathcal{K}_0^{(1)} |G(\phi)\rangle\langle G(\phi)| \mathcal{K}_0^{(1)} + \mathcal{K}_1^{(1)} |G(\phi)\rangle\langle G(\phi)| \mathcal{K}_1^{(1)} \\ &= \frac{1}{2} \left\{ \begin{pmatrix} \cos^2 \phi' & 0 \\ 0 & \sin^2 \phi' \end{pmatrix} \otimes (|+\rangle\langle +|)^{\otimes(N-1)} \right. \\ &\quad + e^{-2i\phi'(N-1)} \frac{i}{2} \sin(2\phi') \sigma_z \otimes (|+\rangle\langle -|)^{\otimes(N-1)} \\ &\quad + e^{2i\phi'(N-1)} \frac{-i}{2} \sin(2\phi') \sigma_z \otimes (|-\rangle\langle +|)^{\otimes(N-1)} \\ &\quad \left. + \begin{pmatrix} \sin^2 \phi' & 0 \\ 0 & \cos^2 \phi' \end{pmatrix} \otimes (|-\rangle\langle -|)^{\otimes(N-1)} \right\}, \end{aligned} \quad (33)$$

Continuously we calculate  $\rho_2(\phi)$  as:

$$\begin{aligned} \rho_2(\phi) &= \mathcal{K}_0^{(2)} \rho_1(\phi) \mathcal{K}_0^{(2)} + \mathcal{K}_1^{(2)} \rho_1(\phi) \mathcal{K}_1^{(2)} \\ &= \frac{1}{4} \left\{ \begin{aligned} &\left( \begin{array}{cc} \cos^2 \phi' & 0 \\ 0 & \sin^2 \phi' \end{array} \right) \otimes I \otimes (|+\rangle\langle+|)^{\otimes(N-2)} \\ &+ e^{-2i\phi'(N-1)} \frac{i}{2} \sin(2\phi') \sigma_z \otimes \sigma_z \otimes (|+\rangle\langle-|)^{\otimes(N-2)} \\ &+ e^{2i\phi'(N-1)} \frac{-i}{2} \sin(2\phi') \sigma_z \otimes \sigma_z \otimes (|-\rangle\langle+|)^{\otimes(N-2)} \\ &+ \left( \begin{array}{cc} \sin^2 \phi' & 0 \\ 0 & \cos^2 \phi' \end{array} \right) \otimes I \otimes (|-\rangle\langle-|)^{\otimes(N-2)} \end{aligned} \right\}, \end{aligned} \quad (34)$$

and so on. Finally, we get

$$\rho_N(\phi) = \frac{1}{2^N} \left( I^{\otimes N} + \sin(\phi) \sin[(N-1)\phi] \sigma_z^{\otimes N} \right). \quad (35)$$

To calculate the QFI, we use Eq. (7) in the main text with  $\rho_N(\phi) = \sum_k \ell_k |\ell_k\rangle\langle\ell_k|$ , and get

$$Q = 2 \sum_{i,j,\ell_i+\ell_j \neq 0} \frac{|\langle\ell_i|\partial_\phi \rho_N(\phi)|\ell_j\rangle|^2}{\ell_i + \ell_j} = (N-1)^2, \quad (36)$$

where we first calculated  $\partial_\phi \rho_N(\phi)$  from Eq. (35), and then used  $\phi = \pi/2$ .

## 2. For GHZ state

We consider the case where the initial probe state is a GHZ state. For the generator  $\mathcal{H}_\phi = J_x = \frac{1}{2} \sum_{k=1}^N \sigma_x^{(k)}$ , the defined GHZ state in Eq. (9) explicitly gives:

$$|\psi_{\text{GHZ}}\rangle = \frac{1}{\sqrt{2}} \left( |+\rangle^{\otimes N} + |-\rangle^{\otimes N} \right), \quad (37)$$

where  $|\pm\rangle^{\otimes N}$  are eigenstates of  $\mathcal{H}_\phi$  corresponds to the maximum and minimum eigenvalues. This state can be prepared from a star-graph state by adding a Hadamard gate into the first qubits of Eq. (25).

We first compute two terms  $\mathcal{H}_\phi |\psi_{\text{GHZ}}\rangle$  and  $\mathcal{H}_\phi^2 |\psi_{\text{GHZ}}\rangle$ , where

$$\begin{aligned} \mathcal{H}_\phi |\psi_{\text{GHZ}}\rangle &= \left[ \frac{1}{2} \sum_{k=1}^N \sigma_x^{(k)} \right] \frac{1}{\sqrt{2}} \left( |+\rangle^{\otimes N} + |-\rangle^{\otimes N} \right) \\ &= \frac{N}{2\sqrt{2}} \left( |+\rangle^{\otimes N} - |-\rangle^{\otimes N} \right), \end{aligned} \quad (38)$$

and

$$\mathcal{H}_\phi^2 |\psi_{\text{GHZ}}\rangle = \frac{N^2}{4} |\psi_{\text{GHZ}}\rangle. \quad (39)$$

Then, we obtain  $\langle\psi_{\text{GHZ}}|\mathcal{H}_\phi|\psi_{\text{GHZ}}\rangle = 0$  and  $\langle\psi_{\text{GHZ}}|\mathcal{H}_\phi^2|\psi_{\text{GHZ}}\rangle = N^2/4$ . Finally, the QFIM yields

$$\begin{aligned} Q_{\text{GHZ}} &= 4 \left[ \langle\psi_{\text{GHZ}}|\mathcal{H}_\phi^2|\psi_{\text{GHZ}}\rangle - (\langle\psi_{\text{GHZ}}|\mathcal{H}_\phi|\psi_{\text{GHZ}}\rangle)^2 \right] \\ &= N^2. \end{aligned} \quad (40)$$

Similarly, for noisy cases, we have  $Q_{\text{GHZ}} = N^2$ .

## C. Deriving QFIM for multiparameter estimation

The QFIM for a pure star graph state is given by

$$Q_{\alpha\beta} = \frac{1}{2} \langle G(\phi) | (L_\alpha L_\beta + L_\beta L_\alpha) | G(\phi) \rangle, \quad (41)$$

where  $L$  is given in the symmetric logarithmic derivative (SLD) as

$$L_\alpha = 2(|\partial_{\phi_\alpha} G(\phi)\rangle\langle G(\phi)| + |G(\phi)\rangle\langle\partial_{\phi_\alpha} G(\phi)|). \quad (42)$$

For concreteness, we first derive

$$\begin{aligned} |\partial_{\phi_\alpha} G(\phi)\rangle &= \partial_{\phi_\alpha} \mathcal{U}(\phi) |G\rangle \\ &= \partial_{\phi_\alpha} e^{-it\mathcal{H}} |G\rangle \\ &= -i \int_0^t du e^{-i(1-u)\mathcal{H}} [\partial_{\phi_\alpha} \mathcal{H}] e^{-iu\mathcal{H}} |G\rangle \\ &= -ie^{-i\mathcal{H}} \int_0^t du e^{iu\mathcal{H}} J_\alpha e^{-iu\mathcal{H}} |G\rangle \\ &= -i\mathcal{U}(\phi) \mathcal{A}_\alpha |G\rangle, \end{aligned} \quad (43)$$

where  $\mathcal{H}$  is given in Eq. (2), and

$$\mathcal{A}_\alpha = \int_0^t du e^{iu\mathcal{H}} J_\alpha e^{-iu\mathcal{H}}, \quad (44)$$

is a Hermitian operator [45, 61].

Then, the SLD (42) and QFIM (41) are explicitly given as

$$L_\alpha = 2i\mathcal{U}(\phi) [|G\rangle\langle G|, \mathcal{A}_\alpha] \mathcal{U}^\dagger(\phi), \quad (45)$$

$$Q_{\alpha\beta} = 4\text{Re}[\langle G | \mathcal{A}_\alpha \mathcal{A}_\beta | G \rangle - \langle G | \mathcal{A}_\alpha | G \rangle \langle G | \mathcal{A}_\beta | G \rangle]. \quad (46)$$

In quantum circuits, the QFIM can be calculated using a stochastic method [60].

For a general mixed state, such as a star graph under noise, i.e.,  $\rho(\phi, \gamma) = \sum_k \ell_k |\ell_k\rangle\langle\ell_k|$ , the QFIM gives

$$Q_{\alpha\beta} = 2 \sum_{i,j,\ell_i+\ell_j \neq 0} \frac{\langle\ell_i|\partial_{\phi_\alpha} \rho(\phi, \gamma)|\ell_j\rangle \langle\ell_j|\partial_{\phi_\beta} \rho(\phi, \gamma)|\ell_i\rangle}{\ell_i + \ell_j}. \quad (47)$$

The QCRB in this case is given by  $C_Q = \text{Tr}[Q^{-1}]$ .

## D. Noisy QFI of graph states

In this section, we examine how different types of noise impact the QFI. In addition to dephasing, we also encounter bit flip, phase flip, and depolarizing. The relevant Kraus operators are as follows:

$$\begin{aligned} K_0 &= \sqrt{1-\gamma} \begin{pmatrix} 1 & 0 \\ 0 & 1 \end{pmatrix}; K_1 = \sqrt{\gamma} \begin{pmatrix} 0 & 1 \\ 1 & 0 \end{pmatrix}, \text{ for bit flip,} \\ K_0 &= \sqrt{1-\gamma} \begin{pmatrix} 1 & 0 \\ 0 & 1 \end{pmatrix}; K_1 = \sqrt{\gamma} \begin{pmatrix} 1 & 0 \\ 0 & -1 \end{pmatrix}, \text{ for phase flip,} \\ K_0 &= \sqrt{1-\gamma} \begin{pmatrix} 1 & 0 \\ 0 & 1 \end{pmatrix}; K_1 = \sqrt{\gamma/3} \begin{pmatrix} 0 & 1 \\ 1 & 0 \end{pmatrix}; K_2 = \end{aligned}$$



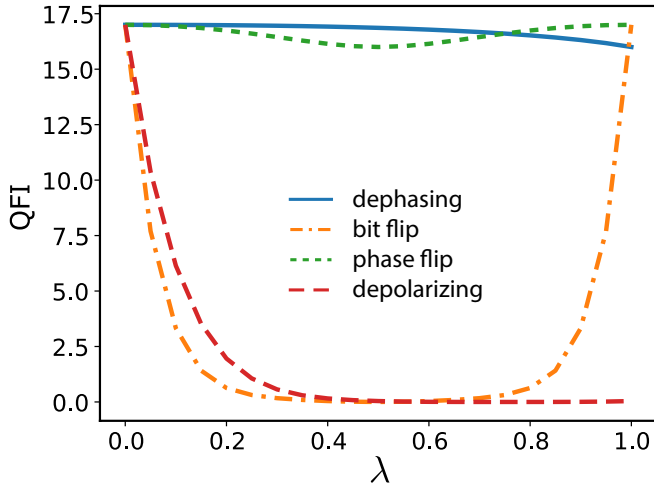


FIG. 7. QFI under different noises.

$\sqrt{\gamma/3} \begin{pmatrix} 0 & -i \\ i & 0 \end{pmatrix}; K_3 = \sqrt{\gamma/3} \begin{pmatrix} 1 & 0 \\ 0 & -1 \end{pmatrix}$ , for depolarizing, where  $\gamma \in [0, 1]$  the noise probability. The QFI is shown in Fig. 7, with different noises.

### E. Bayes Inference

We start from the final state

$$\rho_N(\phi) = \frac{1}{2^N} \left( I^{\otimes N} + \sin(\phi) \sin[(N-1)\phi] \sigma_z^{\otimes N} \right), \quad (48)$$

when  $\lambda = 1$ . Because  $\sigma_z^{\otimes N}$  has the same numbers of component +1 and -1, the state would contain the same number of components  $1 + \sin(\phi) \sin[(N-1)\phi]$  and  $1 - \sin(\phi) \sin[(N-1)\phi]$  on the diagonal. Therefore

$$\begin{aligned} P(D|\phi) &= \prod_{k=1}^{2^N} \text{Tr} \left[ \rho_N(\phi) |k\rangle \langle k| \right] \\ &= \frac{1}{2^{N \cdot (2^N)}} \left[ (1 + \sin(\phi) \sin[(N-1)\phi])^{2^{(N-1)}} (1 - \sin(\phi) \sin[(N-1)\phi])^{2^{(N-1)}} \right] \\ &= \frac{1}{2^{N \cdot (2^N)}} \left[ 1 - \sin^2(\phi) \sin^2[(N-1)\phi] \right]^{2^{(N-1)}} \\ &= \frac{1}{2^{N \cdot (2^N)}} \sum_{k=0}^{2^{N-1}} \binom{2^{N-1}}{k} (-1)^k \sin^{2k}(\phi) \sin^{2k}[(N-1)\phi], \end{aligned} \quad (49)$$

And then  $P(\phi|D)$  is

$$\begin{aligned} P(\phi|D) &= \int P(D|\phi) d\phi = \frac{1}{2^{N \cdot (2^N)}} \int \sum_{k=0}^{2^{N-1}} \binom{2^{N-1}}{k} (-1)^k \sin^{2k}(\phi) \sin^{2k}[(N-1)\phi] d\phi \\ &= \frac{1}{2^{N \cdot (2^N)}} \sum_{k=0}^{2^{N-1}} \binom{2^{N-1}}{k} (-1)^k \int \sin^{2k}(\phi) \sin^{2k}[(N-1)\phi] d\phi. \end{aligned} \quad (50)$$

Finally, we obtain

$$\phi_{\text{estimated}} = \int \phi P(\phi|D) d\phi. \quad (51)$$

The integrals in Eqs. (50, 51) are derived numerically.

## V. CONCLUSION

This study focuses on precise measurement techniques in noisy quantum systems. By using graph-state resources, we developed a method that enhances measurement accuracy and resilience against noise. Particularly, we used graph-state resources for robust quantum magnetometry under noise and showed promise for overcoming

practical measurement challenges. Our demonstrations highlight significant advancements in accurately measuring both single and multiple Larmor frequencies. These outcomes showcase a spectrum ranging from surpassing the standard quantum limit to achieving Heisenberg scaling, marking significant progress.

These advancements are crucial across quantum computing, communication, and sensing, where precise measurements are indispensable. The capability to achieve high-precision measurements despite noise underscores the reliability and efficiency of quantum technologies. Further research in graph state-based quantum metrology could revolutionize various fields and pave the way for practical quantum technologies despite noise. We remark that with advancements in experimental generation of arbitrary photonic graph states via atomic [62] sources, and quantum-error-correcting code based on graph states [63], this line of research will provide a theoretical basis for quantum-metrological advantages through experiments with graph states.

#### DATA AVAILABILITY

Data are available from the corresponding authors upon reasonable request.

#### CODE AVAILABILITY

All codes used to produce the findings of this study are incorporated into `qtix` [64, 65] and available at:

<https://github.com/echkon/tqix-developers>.

#### ACKNOWLEDGEMENTS

This work is supported by JSPS KAKENHI Grant Number 23K13025.

#### AUTHOR CONTRIBUTIONS STATEMENT

P.T.N and T.K.L. wrote the initial code and implemented the numerical simulation. L.B.H. derived the theoretical framework, implemented the numerical simulation, and analyzed the results. L.B.H. and H.Q.N supervised the work. All authors discussed and wrote the manuscript.

#### COMPETING INTERESTS

The author declares no competing interests.

- 
- [1] C. L. Degen, F. Reinhard, and P. Cappellaro, *Rev. Mod. Phys.* **89**, 035002 (2017).
- [2] T. Chalopin, C. Bouazza, A. Evrard, V. Makhalov, D. Dreon, J. Dalibard, L. A. Sidorenkov, and S. Nascimbene, *Nature Communications* **9**, 4955 (2018).
- [3] L. Pezzè, A. Smerzi, M. K. Oberthaler, R. Schmied, and P. Treutlein, *Rev. Mod. Phys.* **90**, 035005 (2018).
- [4] L. B. Ho and Y. Kondo, *Physics Letters A* **383**, 153 (2019).
- [5] N. Friis, D. Orsucci, M. Skotiniotis, P. Sekatski, V. Dunjko, H. J. Briegel, and W. Dür, *New Journal of Physics* **19**, 063044 (2017).
- [6] N. Shettell and D. Markham, *Phys. Rev. Lett.* **124**, 110502 (2020).
- [7] Y. Wang and K. Fang, *Phys. Rev. A* **102**, 052601 (2020).
- [8] T. K. Le, H. Q. Nguyen, and L. B. Ho, *Scientific Reports* **13**, 17775 (2023).
- [9] A. Niezgoda and J. Chwedeńczuk, *Phys. Rev. Lett.* **126**, 210506 (2021).
- [10] Y. Chu, X. Li, and J. Cai, *Phys. Rev. Lett.* **130**, 170801 (2023).
- [11] I. Avdic, L. M. Sager-Smith, I. Ghosh, O. C. Wedig, J. S. Higgins, G. S. Engel, and D. A. Mazziotti, *Phys. Rev. Res.* **5**, 043097 (2023).
- [12] Z. Zhang and L. M. Duan, *New Journal of Physics* **16**, 103037 (2014).
- [13] L. Maccone and A. Ricciardi, *Quantum* **4**, 292 (2020).
- [14] M. Gessner, A. Smerzi, and L. Pezzè, *Nature Communications* **11**, 3817 (2020).
- [15] C. Troullinou, V. G. Lucivero, and M. W. Mitchell, *Phys. Rev. Lett.* **131**, 133602 (2023).
- [16] V. Cimini, I. Gianani, N. Spagnolo, F. Leccese, F. Sciarino, and M. Barbieri, *Phys. Rev. Lett.* **123**, 230502 (2019).
- [17] K. Jung, M. H. Abobeih, J. Yun, G. Kim, H. Oh, A. Henry, T. H. Taminiau, and D. Kim, *npj Quantum Information* **7**, 41 (2021).
- [18] N. F. Costa, Y. Omar, A. Sultanov, and G. S. Paraoanu, *EPJ Quantum Technology* **8**, 16 (2021).
- [19] V. Cimini, M. Valeri, E. Polino, S. Piacentini, F. Ceccarelli, G. Corrielli, N. Spagnolo, R. Osellame, and F. Sciarrino, *Advanced Photonics* **5**, 016005 (2023).
- [20] E. Rinaldi, M. G. Lastre, S. G. Herreros, S. Ahmed, M. Khanahmadi, F. Nori, and C. S. Muñoz, “Parameter estimation by learning quantum correlations in continuous photon-counting data using neural networks,” (2023), [arXiv:2310.02309](https://arxiv.org/abs/2310.02309) [quant-ph].

- [21] E. M. Kessler, I. Lovchinsky, A. O. Sushkov, and M. D. Lukin, *Phys. Rev. Lett.* **112**, 150802 (2014).
- [22] N. Shettell, W. J. Munro, D. Markham, and K. Nemoto, *New Journal of Physics* **23**, 043038 (2021).
- [23] K. Yamamoto, S. Endo, H. Hakoshima, Y. Matsuzaki, and Y. Tokunaga, *Phys. Rev. Lett.* **129**, 250503 (2022).
- [24] I. Rojkov, D. Layden, P. Cappellaro, J. Home, and F. Reiter, *Phys. Rev. Lett.* **128**, 140503 (2022).
- [25] T. J. Proctor, P. A. Knott, and J. A. Dunningham, *Phys. Rev. Lett.* **120**, 080501 (2018).
- [26] M. T. Rahim, A. Khan, U. Khalid, J. u. Rehman, H. Jung, and H. Shin, *Scientific Reports* **13**, 11630 (2023).
- [27] B. Koczor, S. Endo, T. Jones, Y. Matsuzaki, and S. C. Benjamin, *New Journal of Physics* **22**, 083038 (2020).
- [28] X. Yang, X. Chen, J. Li, X. Peng, and R. Laflamme, *Scientific Reports* **11**, 672 (2021).
- [29] R. Kaubruegger, D. V. Vasilyev, M. Schulte, K. Hammerer, and P. Zoller, *Phys. Rev. X* **11**, 041045 (2021).
- [30] J. J. Meyer, J. Borregaard, and J. Eisert, *npj Quantum Information* **7**, 89 (2021).
- [31] C. D. Marciniak, T. Feldker, I. Pogorelov, R. Kaubruegger, D. V. Vasilyev, R. van Bijnen, P. Schindler, P. Zoller, R. Blatt, and T. Monz, *Nature* **603**, 604 (2022).
- [32] R. Kaubruegger, A. Shankar, D. V. Vasilyev, and P. Zoller, *PRX Quantum* **4**, 020333 (2023).
- [33] E. Portolés, S. Iwakiri, G. Zheng, P. Rickhaus, T. Taniguchi, K. Watanabe, T. Ihn, K. Ensslin, and F. K. de Vries, *Nature Nanotechnology* **17**, 1159 (2022).
- [34] M. Gulka, D. Wirtitsch, V. Ivády, J. Vodnik, J. Hruby, G. Magchies, E. Bourgeois, A. Gali, M. Trupke, and M. Nesladek, *Nature Communications* **12**, 4421 (2021).
- [35] J. J. Carmiggelt, I. Bertelli, R. W. Mulder, A. Teepe, M. Elyasi, B. G. Simon, G. E. W. Bauer, Y. M. Blanter, and T. van der Sar, *Nature Communications* **14**, 490 (2023).
- [36] W. S. Huxter, M. L. Palm, M. L. Davis, P. Welter, C.-H. Lambert, M. Trassin, and C. L. Degen, *Nature Communications* **13**, 3761 (2022).
- [37] O. Sahin, E. de Leon Sanchez, S. Conti, A. Akkiraju, P. Reshetikhin, E. Druga, A. Aggarwal, B. Gilbert, S. Bhave, and A. Ajoy, *Nature Communications* **13**, 5486 (2022).
- [38] C. L. Garrido Alzar, *AVS Quantum Science* **1**, 014702 (2019), [https://pubs.aip.org/avs/aqs/article-pdf/doi/10.1116/1.5120348/14571801/014702\\_1.online.pdf](https://pubs.aip.org/avs/aqs/article-pdf/doi/10.1116/1.5120348/14571801/014702_1.online.pdf).
- [39] P. Kumar, F. Fabre, A. Durand, T. Clua-Provost, J. Li, J. Edgar, N. Rougemaille, J. Coraux, X. Marie, P. Renucci, C. Robert, I. Robert-Philip, B. Gil, G. Cassabois, A. Finco, and V. Jacques, *Phys. Rev. Appl.* **18**, L061002 (2022).
- [40] M. Hein, W. Dür, J. Eisert, R. Raussendorf, M. V. den Nest, and H.-J. Briegel, “Entanglement in graph states and its applications,” in *Proceedings of the International School of Physics “Enrico Fermi”*, Ebook Volume 162: Quantum Computers, Algorithms and Chaos (IOS Press, 2006) pp. 115–218.
- [41] M. Hein, J. Eisert, and H. J. Briegel, *Phys. Rev. A* **69**, 062311 (2004).
- [42] B. A. Bell, D. A. Herrera-Martí, M. S. Tame, D. Markham, W. J. Wadsworth, and J. G. Rarity, *Nature Communications* **5**, 3658 (2014).
- [43] D. Schlingemann and R. F. Werner, *Phys. Rev. A* **65**, 012308 (2001).
- [44] B. A. Bell, D. Markham, D. A. Herrera-Martí, A. Marin, W. J. Wadsworth, J. G. Rarity, and M. S. Tame, *Nature Communications* **5**, 5480 (2014).
- [45] L. B. Ho, H. Hakoshima, Y. Matsuzaki, M. Matsuzaki, and Y. Kondo, *Phys. Rev. A* **102**, 022602 (2020).
- [46] L. Pezzé and A. Smerzi, *Phys. Rev. Lett.* **102**, 100401 (2009).
- [47] V. Giovannetti, S. Lloyd, and L. Maccone, *Science* **306**, 1330 (2004), <https://www.science.org/doi/pdf/10.1126/science.1104149>.
- [48] V. Giovannetti, S. Lloyd, and L. Maccone, *Phys. Rev. Lett.* **96**, 010401 (2006).
- [49] S. F. Huelga, C. Macchiavello, T. Pellizzari, A. K. Ekert, M. B. Plenio, and J. I. Cirac, *Phys. Rev. Lett.* **79**, 3865 (1997).
- [50] A. Smirne, J. Kołodyński, S. F. Huelga, and R. Demkowicz-Dobrzański, *Phys. Rev. Lett.* **116**, 120801 (2016).
- [51] Y. Matsuzaki, S. C. Benjamin, and J. Fitzsimons, *Phys. Rev. A* **84**, 012103 (2011).
- [52] A. W. Chin, S. F. Huelga, and M. B. Plenio, *Phys. Rev. Lett.* **109**, 233601 (2012).
- [53] T. Tanaka, P. Knott, Y. Matsuzaki, S. Dooley, H. Yamaguchi, W. J. Munro, and S. Saito, *Phys. Rev. Lett.* **115**, 170801 (2015).
- [54] P. Tekely, *Magnetic Resonance in Chemistry* **40**, 800 (2002).
- [55] M. A. Nielsen and I. L. Chuang, *Quantum Computation and Quantum Information* (Cambridge University Press, Cambridge, UK, 2010).
- [56] M. G. A. PARIS, *International Journal of Quantum Information* **07**, 125 (2009), <https://doi.org/10.1142/S0219749909004839>.
- [57] W. Dür, H. Aschauer, and H.-J. Briegel, *Phys. Rev. Lett.* **91**, 107903 (2003).
- [58] G. E. Uhlenbeck and L. S. Ornstein, *Phys. Rev.* **36**, 823 (1930).
- [59] T. Yu and J. Eberly, *Optics Communications* **283**, 676 (2010), quo vadis Quantum Optics?
- [60] L. B. Ho, *EPJ Quantum Technology* **10**, 37 (2023).
- [61] R. M. Wilcox, *Journal of Mathematical Physics* **8**, 962 (2004), [https://pubs.aip.org/aip/jmp/article-pdf/8/4/962/7440792/962\\_1.online.pdf](https://pubs.aip.org/aip/jmp/article-pdf/8/4/962/7440792/962_1.online.pdf).
- [62] P. Thomas, L. Ruscio, O. Morin, and G. Rempe, *Nature* **608**, 677–681 (2022).
- [63] C. Vigliar, S. Paesani, Y. Ding, J. C. Adcock, J. Wang, S. Morley-Short, D. Bacco, L. K. Oxenløwe, M. G. Thompson, J. G. Rarity, and A. Laing, *Nature Physics* **17**, 1137–1143 (2021).
- [64] N. T. Viet, N. T. Chuong, V. T. N. Huyen, and L. B. Ho, *Computer Physics Communications* **286**, 108686 (2023).
- [65] L. B. Ho, K. Q. Tuan, and H. Q. Nguyen, *Computer Physics Communications* **263**, 107902 (2021).